Waveform inversion of synthetic reflection data for VTI attenuation parameters

Tong Bai[1], Ilya Tsvankin[1] and Xinming Wu[2]
1. Center for Wave Phenomena, Colorado School of Mines
2. University of Texas at Austin

ABSTRACT
In a previous project report, we proposed a waveform inversion (WI) algorithm for attenuation analysis in heterogeneous VTI (transversely isotropic with a vertical symmetry axis) media. Here, we supplement that method with the local similarity technique designed to remove the time shifts between the simulated and observed data. In the presence of velocity errors, this technique substantially stabilizes computation of the WI gradients and improves parameter estimation. The gradients are derived with the adjoint-state method, and four parameters describing the attenuation of P- and SV-waves are updated simultaneously. The algorithm is applied to multicomponent reflection data generated for a modified section of the BP TI model. The inversion significantly reduces the data misfit and recovers the long-wavelength components of the attenuation parameters, especially in the upper part of the section. Synthetic testing also shows that the inversion algorithm remains stable when the data are contaminated by mild Gaussian noise.

Key words: waveform inversion, time domain, attenuation, anisotropy

1 INTRODUCTION

Seismic reflection data are substantially distorted by intrinsic attenuation in the subsurface. The loss of high frequencies in attenuative media limits the bandwidth of recorded wavefields and the resolution of seismic inversion. Therefore, reliable estimation of attenuation and compensation for its influence can improve most seismic processing steps including amplitude-variation-with-offset (AVO) analysis and depth imaging. In addition, attenuation coefficients provide useful complementary information in reservoir characterization and can be used in fluid detection and evaluation of permeability (Donald et al., 2004; Carcione et al., 2010; Müller et al., 2010).

Attenuation coefficients often exhibit strong directional dependence, or attenuation anisotropy (Zhu et al., 2006; Best et al., 2007; Chichinina et al., 2009). Krzikalla and Müller (2011) combine anisotropic Backus limits with interlayer flow models to characterize the anisotropic attenuation coefficients of P- and SV-waves in thinly layered porous rocks. Numerical and laboratory experiments have confirmed the link between attenuation anisotropy and parameters of fracture networks (Chichinina et al., 2006; Rao and Wang, 2009; Ekanem et al., 2013; Guo and McMechan, 2017).

The quality factor can be estimated, for instance, by the frequency-shift (FSM) and spectral-ratio (SRM) methods, which utilize the frequency dependence of attenuation coefficients (e.g., Quan and Harris, 1997; Sams and Goldberg, 1990). However, the conventional methods are generally limited to structurally simple models and suffer from several implementation problems, such as sensitivity to noise and to event interference (de Castro Nunes et al., 2011).

Waveform inversion (WI) has proved to be an efficient tool for building high-resolution velocity models. Recent developments include extension of WI to anisotropic and/or elastic media (Lee et al., 2010; Kamath and Tsvankin, 2016; Owusu et al., 2016), which involves multiparameter inversion. Analysis of radiation patterns (Gholami et al., 2010; Operto et al., 2013; Alkhalifah and Plessix, 2014) helps identify parameter trade-offs and devise optimal parameterizations for different sets of input data.

The influence of attenuation on both amplitude and phase of seismic waves makes it an essential component of WI. Proper compensation for attenuation can significantly increase the accuracy of the inverted velocity parameters (Causse et al., 1999; Kurzmann et al., 2013; Xue et al., 2016). Furthermore, WI potentially represents a powerful tool for attenuation analysis. Some existing algorithms adopt a hierarchical strategy, in which the velocity field is recovered before attenuation estimation (Kamei and Pratt, 2008; Prieux et al., 2013). Other implementations of WI for attenuative media rely on a priori knowledge of the velocity parameters (Bai and Yingst, 2013).

Using a finite-difference simulator for anisotropic atten-

uative models (Bai and Tsvankin, 2016a), Bai and Tsvankin (2016b) propose a time-domain WI algorithm for attenuation analysis in VTI media. The gradients of the objective function with respect to the attenuation parameters are derived using the adjoint-state method. The four parameters describing the attenuation of P- and SV-waves in VTI models are updated simultaneously. Bai and Tsvankin (2016b) test the algorithm on transmission data for models with a Gaussian anomaly in one of the Thomsen-style attenuation parameters.

Here, we refine the methodology of Bai and Tsvankin (2016b) by implementing the local similarity technique, designed to mitigate the influence of velocity errors on the inversion, and test the algorithm on a more realistic synthetic data set. First, we briefly review the methodology of time-domain modeling and WI in anisotropic attenuative media. Next, the inversion algorithm is applied to reflection data generated for a modified section of the BP TI model. Then, we assess the influence of inaccurate velocity parameters on the WI results and show that the local-similarity technique represents a viable tool for reducing the impact of velocity errors. Finally, a test on noise-contaminated data illustrates the stability of parameter estimation in the presence of Gaussian noise.

2 METHODOLOGY

2.1 Forward modeling for viscoelastic VTI media

We model wave propagation in viscoelastic VTI media with a time-domain finite-difference code (Bai and Tsvankin, 2016a). For purposes of computational efficiency, only one relaxation mechanism is employed, which proves to be sufficient for nearly constant-Q simulation within the frequency band typical for surface seismic surveys (Zhu et al., 2013).

The relaxation function for general anisotropic attenuative media can be found in Bai and Tsvankin (2016a). For a single relaxation mechanism, that function has the form:

$$\Psi_{ijkl}(t) = C^R_{ijkl}\,\left(1+\tau_{ijkl}\,e^{-t/\tau^\sigma}\right)H(t), \qquad (1)$$

where $C^R_{ijkl} = \Psi_{ijkl}(t\rightarrow\infty)$ is called the "relaxed stiffness," τ^σ denotes the stress relaxation time determined by the reference frequency, the τ_{ijkl}-parameters measure the difference between the stress and strain relaxation time (and, therefore, quantify the magnitude of attenuation in anisotropic media), and $H(t)$ is the Heaviside function. The relaxation function at zero time yields the "unrelaxed stiffness":

$$C^U_{ijkl} \equiv \Psi_{ijkl}(t=0) = C^R_{ijkl}(1+\tau_{ijkl}). \qquad (2)$$

The stiffness difference $\Delta C_{ijkl} = C^U_{ijkl} - C^R_{ijkl}$ is proportional to τ_{ijkl} and, therefore, reflects the magnitude of attenuation.

The P- and SV-wave attenuation in VTI media can be described by the Thomsen-style parameters A_{P0}, A_{S0}, ϵ_Q and δ_Q (Zhu and Tsvankin, 2006; Bai and Tsvankin, 2016a). A_{P0} and A_{S0} denote the P- and S-wave attenuation coefficients in the vertical (symmetry-axis) direction, the parameter ϵ_Q quantifies the fractional difference between the horizontal and vertical P-wave attenuation coefficients, and δ_Q controls the curvature of the P-wave attenuation coefficient at the symmetry axis. Combined with the unrelaxed stiffness coefficients C^U_{ijkl} (used as the reference elastic parameters), these attenuation parameters can be converted into the quality-factor elements Q_{ijkl}.

The viscoelastic stress-strain relationship (an extension of Hooke's law to attenuative models) can be expressed as

$$\sigma_{ij} = C^U_{ijkl}\,\epsilon_{kl} + \Delta C_{ijkl}\,r_{kl}, \qquad (3)$$

where r_{kl} are the memory variables, which satisfy the following partial differential equations (Bai and Tsvankin, 2016a):

$$\frac{\partial\, r_{kl}}{\partial t} = -\frac{1}{\tau^\sigma}\left(r_{kl}+\epsilon_{kl}\right). \qquad (4)$$

2.2 Viscoelastic waveform inversion

The inversion algorithm is based on the conventional ℓ_2-norm objective function (e.g., Tarantola, 1988; Tromp et al., 2005):

$$F(\mathbf{m}) = \frac{1}{2}\sum_{r=1}^{N} \parallel \mathbf{u}(x_r,t,\mathbf{m}) - \mathbf{d}(x_r,t) \parallel^2, \qquad (5)$$

where $\mathbf{u}(x_r,t,\mathbf{m})$ and $\mathbf{d}(x_r,t)$ are the simulated and observed data, respectively, $\mathbf{m}$ is the vector of model parameters, r is the receiver index, and t is the time. Summation over sources is implied. By applying the adjoint-state method (Tarantola, 1988; Tromp et al., 2005; Fichtner, 2005), the gradient at each iteration is obtained from only two simulations of wave propagation (one forward and one adjoint). The gradients for the viscoelastic parameters ΔC_{ijkl} can be expressed in the Born approximation as the cross-correlation of the memory variables from the forward simulation with the adjoint strain field (Tarantola, 1988; Bai and Tsvankin, 2016b):

$$\frac{\partial\, F}{\partial\, \Delta C_{ijkl}} = -\sum_{\text{sources}}\int_0^T \frac{\partial u_i^\dagger}{\partial x_j}\,r_{kl}\,dt, \qquad (6)$$

where $\mathbf{u}^\dagger$ denotes the adjoint displacement field.

Following Bai and Tsvankin (2016b), the inversion algorithm operates with the parameters A_{P0}, A_{S0}, A_{Ph}, and A_{Pn}, where A_{Ph} is the P-wave horizontal attenuation coefficient:

$$A_{Ph} = (1+\epsilon_Q)\,A_{P0} \approx \frac{1}{2Q_{11}}, \qquad (7)$$

and A_{Pn} accounts for the attenuation-anisotropy coefficient δ_Q:

$$A_{Pn} = (1+\delta_Q)\,A_{P0}. \qquad (8)$$

The parameter A_{Pn} governs the angular variation of the P-wave attenuation near the symmetry axis, and has a form similar to the weak-anisotropy approximation for the normal-moveout (NMO) velocity for a horizontal VTI layer.

Replacing ϵ_Q and δ_Q by A_{Ph} and A_{Pn} is convenient for WI because all four selected parameters have the same units and similar magnitudes. The gradients for the parameters A_{P0}, A_{S0}, A_{Ph}, and A_{Pn} can be obtained from those for the stiffness differences ΔC_{ijkl} by applying the chain rule (see Bai

and Tsvankin, 2016b). The L-BFGS method is used in parameter updating to scale the gradients by an approximate inverse Hessian matrix.

2.3 Mitigation of velocity errors

Whereas the algorithm is not designed to update the velocity model, it is important to reduce the influence of velocity errors on attenuation estimation. In particular, errors in the velocity field produce shifts between the simulated and observed events. As a result, the objective function in equation 5 may not properly update the attenuation parameters. To address this problem, we estimate the local similarity map (Fomel, 2009; Fomel and Jin, 2009) from the recorded and modeled arrivals and use ray tracing to pick the trend with the global maximum of the similarity values (Fomel, 2009). This helps calculate the time shifts and then align the corresponding events on the simulated and observed traces prior to WI.

The original L2-norm objective function (equation 5) can be modified as

$$F(\mathbf{m}) = \frac{1}{2}\sum_{r=1}^{N} \parallel \mathbf{u}(x_r,t,\mathbf{m}) - \mathbf{S}(x_r,t)\mathbf{d}(x_r,t) \parallel^2, \quad (9)$$

where $\mathbf{S}(x_r,t)$ is a linear interpolation operator that shifts the recorded events based on the local similarity method. The operator $\mathbf{S}(x_r,t)$ is practically independent of the attenuation parameters ($\mathbf{m}$) when the dispersion is relatively weak. Consequently, the gradient with respect to any model (attenuation) parameter m becomes

$$\frac{\partial F(\mathbf{m})}{\partial m} = \sum_{r=1}^{N} \parallel \mathbf{u}(x_r,t,\mathbf{m}) - \mathbf{S}(x_r,t)\mathbf{d}(x_r,t) \parallel \times \frac{\partial \mathbf{u}(x_r,t,\mathbf{m})}{\partial m}. \quad (10)$$

The only difference between equation 10 and the gradient for the original (unshifted) data is in the form of the data residual. Expressions similar to equations 9 and 10 can be found in Luo and Hale (2014) who apply dynamic warping to reduce the influence of velocity errors on least-squares migration.

3 SYNTHETIC EXAMPLES

3.1 Test for surface data

Here the algorithm is tested on surface data simulated for a modified section of the TI model generated by BP (Figure 1). The section is supposed to represent layered sedimentary formations including anisotropic shales. The velocity parameters and density have a spatial distribution similar to that of the attenuation parameters and are not shown here. The tilt of the symmetry axis was set to zero to make the model VTI. At a depth of 0.3 km, we place 30 evenly spaced displacement sources (tilted by 45° from the vertical) which excite a Ricker wavelet with a central frequency of 20 Hz (same as the reference frequency). The receivers, which record both the vertical and horizontal displacements, are located at each grid point at the same depth as the sources (Figure 1(a)). Triangle filtering with a smoothing radius of 25 samples in both the vertical and horizontal directions is applied to obtain initial models of the attenuation parameters suitable for the L-BFGS algorithm (Figure 2).

We keep the TI velocity parameters V_{P0}, V_{S0}, ϵ, and δ and density at the actual values, and invert for A_{P0}, A_{S0}, A_{Ph}, and A_{Pn} simultaneously. After 18 iterations, the objective function is significantly reduced (Figure 3), and the long-wavelength spatial distribution of the attenuation parameters is generally well-recovered (Figure 4). In particular, the parameters A_{P0} and A_{S0} are accurately estimated even in the deeper part of the section (Figure 4(a) and 4(b)). The profiles in Figure 5 illustrate the accuracy of the parameter updates obtained by WI. The estimated A_{P0} and A_{S0} generally follow the trends of the actual profiles, and A_{Ph} is well-resolved down to 5 km. In contrast, the reconstruction of A_{Pn} is less accurate, likely due to the smaller wavefield sensitivity to the attenuation-anisotropy parameter δ_Q.

3.2 Application of the local-similarity technique

The above test is carried out under the assumption that all velocity parameters are known, which is not realistic in practice. To evaluate the sensitivity of the algorithm to velocity errors, we use the model in Figure 1 with distorted P- and S-wave vertical velocities V_{P0} and V_{S0} (set to 95% of the actual values throughout the section), while ϵ and δ remain exact. As expected, the velocity errors produce shifts between the observed and simulated events, leading to distorted adjoint sources (Figure 6(c)) and deterioration in the inversion results (Figure 7).

To mitigate the influence of these shifts on the objective function, we apply the local similarity method described above. After the similarity-based preconditioning, the algorithm generates more accurate adjoint sources (Figure 8(c)) and inversion gradients, which substantially improves the parameter-estimation results (compare Figures 9 and 7).

3.3 Influence of noise

In addition to velocity errors, it is essential to evaluate the sensitivity of the inversion to noise in the input data. Although Lines et al. (2013) show that Q-estimation by WI is only marginally influenced by moderate noise, their model is acoustic, isotropic, and structurally simple.

We add Gaussian noise in the same frequency band as the signal to the observed data for the model in Figure 1 (Figure 10(b)). Although the signal-to-noise ratio reaches about 20, some weak arrivals from deep interfaces are masked by the noise (Figure 10(b)).

Due to the influence of noise, the objective function flattens out at a larger value (compare Figure 11 with Figure 3) and there are distortions (incoherent "patches") in the inverted parameter sections (Figure 12). However, the algorithm was able to recover major low-frequency spatial features of the attenuation parameters. Similar to the noise-free test (Figure 4),

the reconstruction of A_{P0} and A_{S0} is generally more accurate than that of A_{Ph} and, especially, A_{Pn}.

4 CONCLUSIONS

We applied a previously developed WI methodology to attenuation analysis of reflection data from VTI media. A time-domain modeling algorithm produces a nearly constant Q-matrix in the seismic frequency band using one relaxation mechanism. The 2D multicomponent wavefield is simulated with a finite-difference code. Four parameters (A_{P0}, A_{S0}, A_{Ph}, and A_{Pn}) describing the attenuation of P- and SV-waves are updated simultaneously using the adjoint-state method. We also employed the local-similarity technique to reduce the influence of velocity errors on the inversion results.

The algorithm was tested on a section of the BP model, which was converted into VTI. Starting with strongly smoothed fields of the actual attenuation parameters, waveform inversion was able to reduce the data misfit by 70% and reconstruct major long-wavelength features of the attenuation model. The vertical attenuation coefficients A_{P0} and A_{S0} are well-resolved for most of the model, whereas the horizontal coefficient A_{Ph} is constrained only in the upper part of the section. The accuracy in A_{Pn} is lower compared to that of the other parameters.

To examine the influence of velocity errors, we reduced the P- and S-wave vertical velocities by 5%. These errors produce significant time shifts that distort the adjoint sources and inverted parameters. To precondition the recorded data, we estimated the local similarity map and aligned the corresponding observed and simulated events, which significantly improves the inversion results. However, stable parameter estimation still requires a sufficiently accurate velocity model to minimize the trade-off between the contributions of velocity and attenuation to amplitudes.

Finally, we contaminated input data by Gaussian noise with the signal-to-noise ratio about 20. Despite some distortions in the inverted parameters and a larger remaining data misfit, the results are comparable to those for noise-free data.

5 ACKNOWLEDGMENTS

This work was supported by the Consortium Project on Seismic Inverse Methods for Complex Structures at CWP. The reproducible numeric examples in this paper are generated with the Madagascar open-source software package freely available from http:www.ahay.org. We are grateful to the members of the A(nisotropy)-Team at CWP for fruitful discussions and to Andreas Fichtner (ETH) for his helpful suggestions.

REFERENCES

Alkhalifah, T., and R.-É. Plessix, 2014, A recipe for practical full-waveform inversion in anisotropic media: An analytical parameter resolution study: Geophysics, **79**, R91–R101.

Bai, J., and D. Yingst, 2013, Q estimation through waveform inversion: 75th EAGE Conference & Exhibition.

Bai, T., and I. Tsvankin, 2016a, Time-domain finite-difference modeling for attenuative anisotropic media: Geophysics, **81**, C69–C77.

———, 2016b, Waveform inversion for attenuation estimation in anisotropic media: CWP Project Review Report, **CWP-861**, 73–86.

Best, A. I., J. Sothcott, and C. McCann, 2007, A laboratory study of seismic velocity and attenuation anisotropy in near-surface sedimentary rocks: Geophysical Prospecting, **55**, 609–625.

Carcione, J. M., C. Morency, and J. E. Santos, 2010, Computational poroelasticity—A review: Geophysics, **75**, 75A229–75A243.

Causse, E., R. Mittet, and B. Ursin, 1999, Preconditioning of full-waveform inversion in viscoacoustic media: Geophysics, **64**, 130–145.

Chichinina, T., I. Obolentseva, L. Gik, B. Bobrov, and G. Ronquillo-Jarillo, 2009, Attenuation anisotropy in the linear-slip model: Interpretation of physical modeling data: Geophysics, **74**, WB165–WB176.

Chichinina, T., V. Sabinin, and G. Ronquillo-Jarillo, 2006, QVOA analysis: P-wave attenuation anisotropy for fracture characterization: Geophysics, **71**, C37–C48.

de Castro Nunes, B. I., W. E. De Medeiros, A. F. do Nascimento, and J. A. de Morais Moreira, 2011, Estimating quality factor from surface seismic data: a comparison of current approaches: Journal of Applied Geophysics, **75**, 161–170.

Donald, J., S. Butt, and S. Iakovlev, 2004, Adaptation of a triaxial cell for ultrasonic P-wave attenuation, velocity and acoustic emission measurements: International journal of rock mechanics and mining sciences, **41**, 1001–1011.

Ekanem, A., J. Wei, X.-Y. Li, M. Chapman, and I. Main, 2013, P-wave attenuation anisotropy in fractured media: A seismic physical modelling study: Geophysical Prospecting, **61**, 420–433.

Fichtner, A., 2005, The adjoint method in seismology: theory and application to waveform inversion: AGU Fall Meeting Abstracts, 06.

Fomel, S., 2009, Velocity analysis using AB semblance: Geophysical Prospecting, **57**, 311–321.

Fomel, S., and L. Jin, 2009, Time-lapse image registration using the local similarity attribute: Geophysics, **74**, A7–A11.

Gholami, Y., A. Ribodetti, R. Brossier, S. Operto, and J. Virieux, 2010, Sensitivity analysis of full waveform inversion in VTI media: Presented at the 72nd EAGE Conference and Exhibition incorporating SPE EUROPEC 2010.

Guo, P., and G. A. McMechan, 2017, Sensitivity of 3D 3C synthetic seismograms to anisotropic attenuation and velocity in reservoir models: Geophysics, **82**, T79–T95.

Kamath, N., and I. Tsvankin, 2016, Elastic full-waveform inversion for VTI media: Methodology and sensitivity analysis: Geophysics, **81**, no. 2, C53–C68.

Kamei, R., and R. G. Pratt, 2008, Waveform tomography strategies for imaging attenuation structure with cross-hole data: 70th EAGE Conference & Exhibition, F019.

Krzikalla, F., and T. M. Müller, 2011, Anisotropic P-SV-wave dispersion and attenuation due to inter-layer flow in thinly layered porous rocks: Geophysics, **76**, WA135–WA145.

Kurzmann, A., A. Przebindowska, D. Köhn, and T. Bohlen, 2013, Acoustic full waveform tomography in the presence of attenuation: a sensitivity analysis: Geophysical Journal International, **195**, 985–1000.

Lee, H.-Y., J. M. Koo, D.-J. Min, B.-D. Kwon, and H. S. Yoo, 2010, Frequency-domain elastic full waveform inversion for vti media: Geophysical Journal International, **183**, 884–904.

Lines, L. R., F. Vasheghani, and R. P. Bording, 2013, Short Note: Seismic-Q Estimation Using Full Waveform Inversion of Noisy Data – A Feasibility Study: Canadian Journal of Exploration Geophysics, **38**, 15–20.

Luo, S., and D. Hale, 2014, Least-squares migration in the presence of velocity errors: Geophysics, **79**, S153–S161.

Müller, T. M., B. Gurevich, and M. Lebedev, 2010, Seismic wave attenuation and dispersion resulting from wave-induced flow in porous rocks—A review: Geophysics, **75**, 75A147–75A164.

Operto, S., Y. Gholami, V. Prieux, A. Ribodetti, R. Brossier, L. Metivier, and J. Virieux, 2013, A guided tour of multiparameter full-waveform inversion with multicomponent data: From theory to practice: The Leading Edge, **32**, 1040–1054.

Owusu, J. C., O. Podgornova, M. Charara, S. Leaney, A. Campbell, S. Ali, I. Borodin, L. Nutt, and H. Menkiti, 2016, Anisotropic elastic full-waveform inversion of walkaway vertical seismic profiling data from the Arabian Gulf: Geophysical Prospecting, **64**, 38–53.

Prieux, V., R. Brossier, S. Operto, and J. Virieux, 2013, Multiparameter full waveform inversion of multicomponent ocean-bottom-cable data from the Valhall field. Part 1: imaging compressional wave speed, density and attenuation: Geophysical Journal International, **194**, 1640–1664.

Quan, Y., and J. M. Harris, 1997, Seismic attenuation tomography using the frequency shift method: Geophysics, **62**, 895–905.

Rao, Y., and Y. Wang, 2009, Fracture effects in seismic attenuation images reconstructed by waveform tomography: Geophysics, **74**, R25–R34.

Sams, M., and D. Goldberg, 1990, The validity of Q estimates from borehole data using spectral ratios: Geophysics, **55**, 97–101.

Tarantola, A., 1988, Theoretical background for the inversion of seismic waveforms including elasticity and attenuation: Pure and Applied Geophysics, **128**, 365–399.

Tromp, J., C. Tape, and Q. Liu, 2005, Seismic tomography, adjoint methods, time reversal and banana-doughnut kernels: Geophysical Journal International, **160**, 195–216.

Xue, Z., T. Zhu, S. Fomel, and J. Sun, 2016, Q-compensated full-waveform inversion using constant-Q wave equation: SEG Technical Program Expanded Abstracts, 1063–1068.

Zhu, T., J. M. Carcione, and J. M. Harris, 2013, Approximating constant-Q seismic propagation in the time domain: Geophysical Prospecting, **61**, 931–940.

Zhu, Y., and I. Tsvankin, 2006, Plane-wave propagation in attenuative transversely isotropic media: Geophysics, **71**, no. 2, T17–T30.

Zhu, Y., I. Tsvankin, P. Dewangan, and K. van Wijk, 2006, Physical modeling and analysis of P-wave attenuation anisotropy in transversely isotropic media: Geophysics, **72**, no. 1, D1–D7.

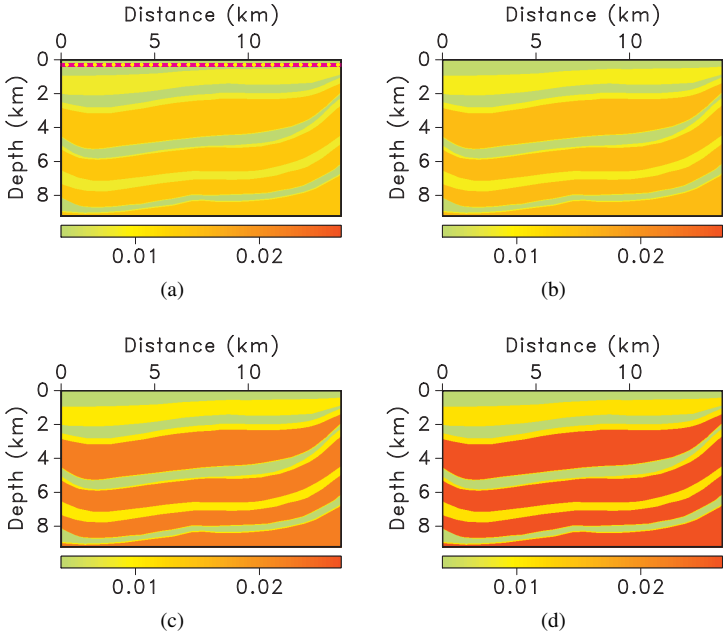

Figure 1. Attenuation parameters for a modified section of the BP TI model: (a) A_{P0}, (b) A_{S0}, (c) A_{Ph}, and (d) A_{Pn}. The symmetry axis is vertical. The model size is 15000 m $\times$ 9250 m, with grid spacing $\Delta x = \Delta z$ =25 m. The yellow dots on plot (a) denote the displacement sources, and the magenta line marks the receivers placed at each grid point.

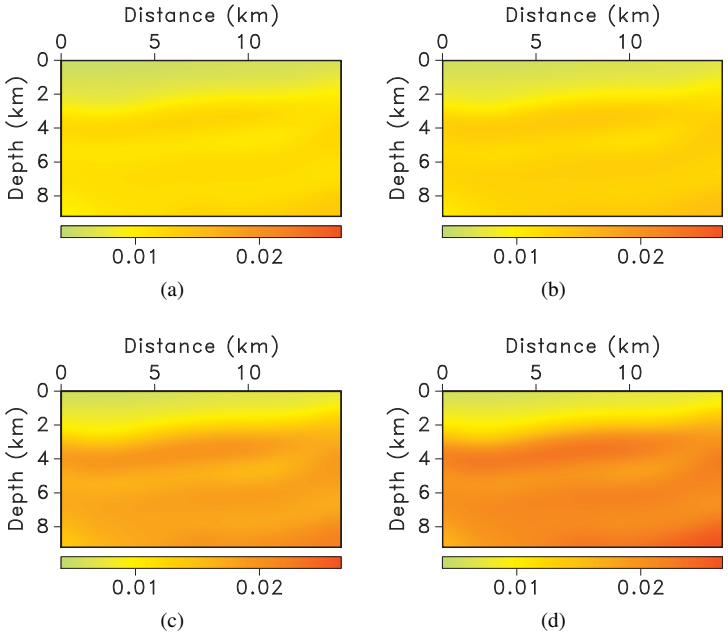

Figure 2. Smoothed actual parameters used as the initial model: (a) A_{P0}, (b) A_{S0}, (c) A_{Ph}, and (d) A_{Pn}.

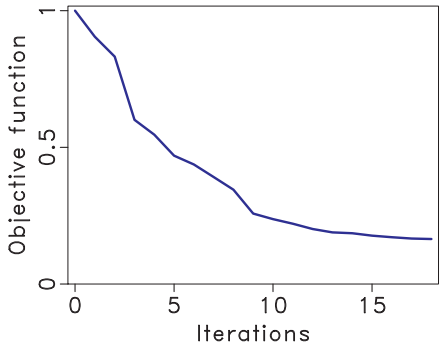

Figure 3. Change of the objective function with iterations for the model in Figure 1.

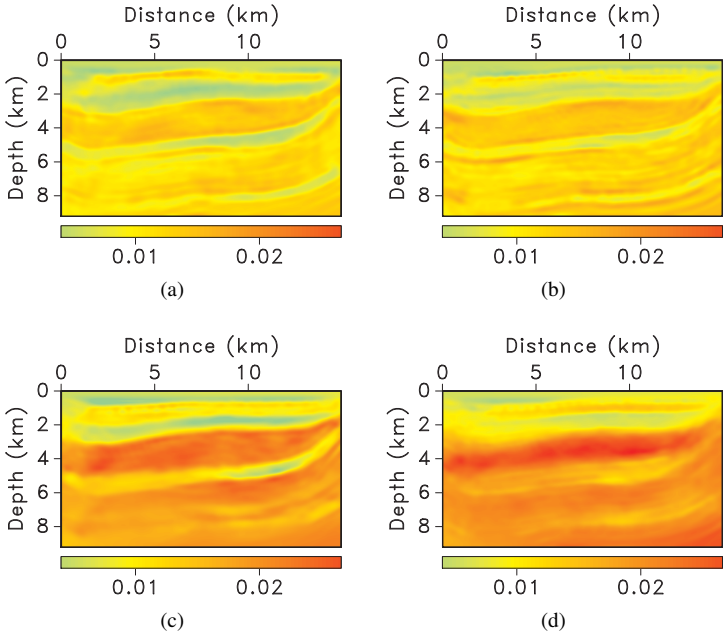

Figure 4. Inverted attenuation parameters: (a) A_{P0}, (b) A_{S0}, (c) A_{Ph}, and (d) A_{Pn}.

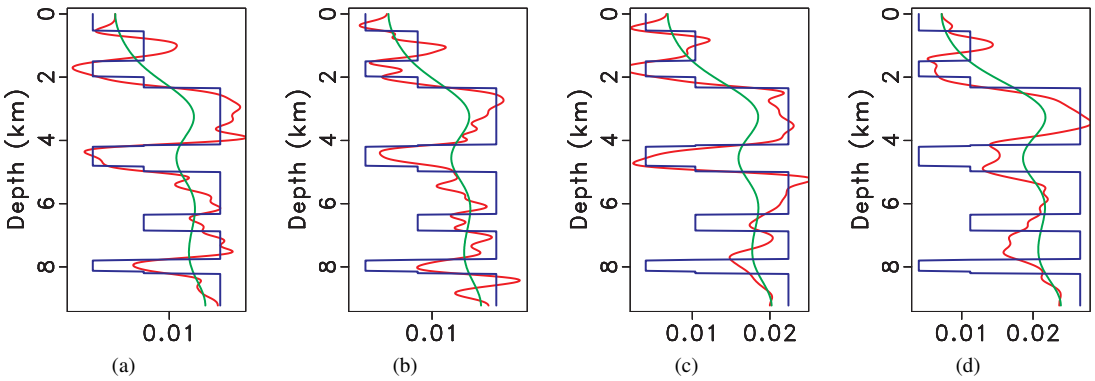

Figure 5. Profiles of the attenuation parameters at $x = 10$ km in Figure 4: (a) A_{P0}, (b) A_{S0}, (c) A_{Ph}, and (d) A_{Pn}. The blue, green, and red lines indicate the actual, initial, and inverted values, respectively.

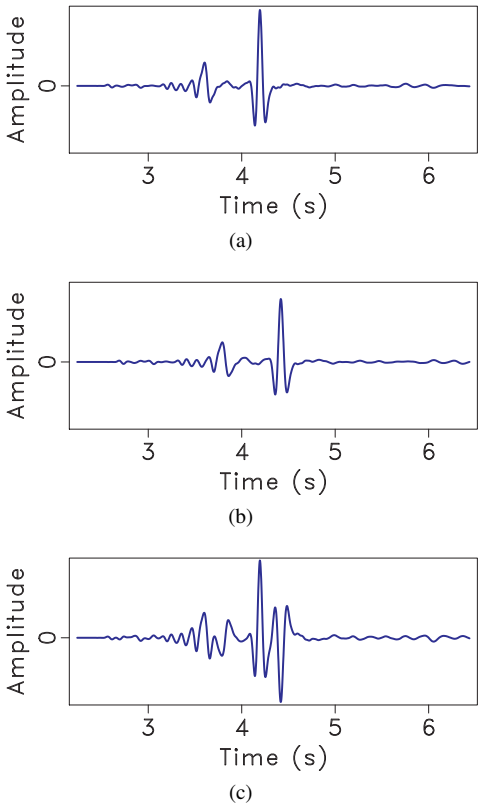

Figure 6. Vertical displacement for the model in Figure 1; the source is located at $x = 0$ and receiver at $x = 7.5$ km. (a) The observed data, (b) the data simulated for the first iteration with an inaccurate velocity model (V_{P0} and V_{S0} are set to 95% of the actual values), (c) the difference between the traces on plots (a) and (b).

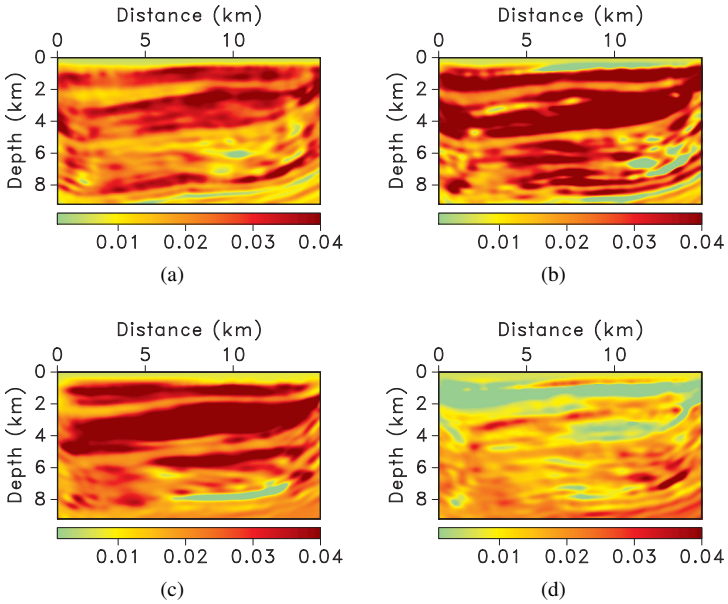

Figure 7. Attenuation parameters estimated with the distorted velocity model: (a) A_{P0}, (b) A_{S0}, (c) A_{Ph}, and (d) A_{Pn}. The upper limit of all parameters (for the L-BFGS algorithm) is set to 0.04, which corresponds to the quality factor close to 12.5.

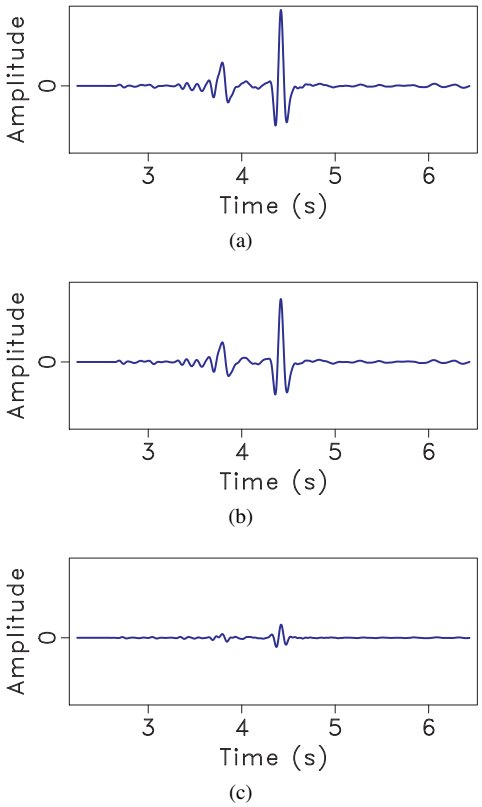

Figure 8. Same as Figure 6, but the observed arrivals on plot (a) are warped (shifted) using the local similarity technique. (b) The data simulated for the first iteration with an inaccurate velocity model (V_{P0} and V_{S0} are set to 95% of the actual values), (c) the difference between the traces on plots (a) and (b).

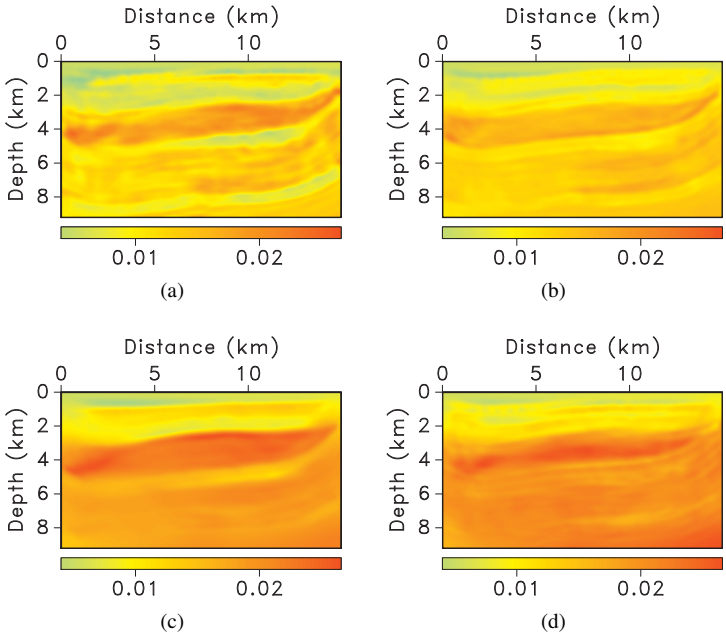

Figure 9. Attenuation coefficients estimated with the distorted velocity model after applying the local similarity technique (Figures 8(a), 8(b), and 8(c)): (a) A_{P0}, (b) A_{S0}, (c) A_{Ph}, and (d) A_{Pn}.

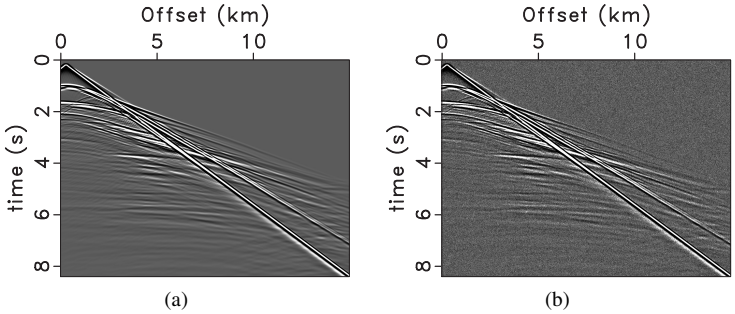

Figure 10. Vertical component of the (a) noise-free and (b) noise-contaminated observed data for the source located at 0.3 km. The noise has the same frequency band as the signal and the signal-to-noise ratio is close to 20.

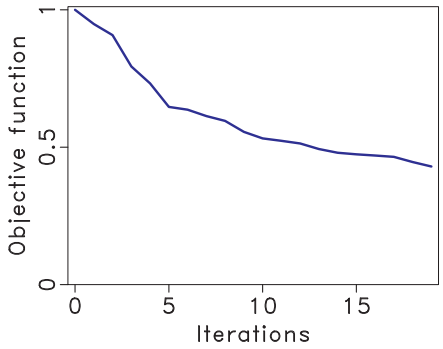

Figure 11. Change of the objective function with iterations for the test with noise-contaminated data.

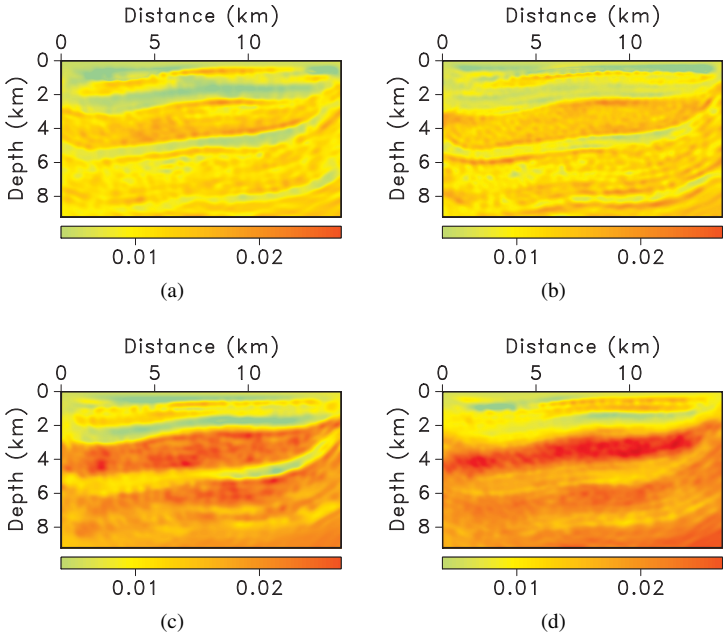

Figure 12. Inverted attenuation parameters for the noise-contaminated data: (a) A_{P0}, (b) A_{S0}, (c) A_{Ph}, and (d) A_{Pn}.